

Single Particle Hopping as an Indicator for Evaluating Electrocatalysts

Jungang Wang

East China Normal University

Linjuan Zhang

Shanghai Institute of Applied Physics, Chinese Academy of Sciences <https://orcid.org/0000-0003-4704-5807>

Jing Xie

Institute of Microelectronics, Chinese Academy of Sciences

Di Li (✉ dli@chem.ecnu.edu.cn)

East China Normal University <https://orcid.org/0000-0003-1674-0110>

Article

Keywords:

Posted Date: January 7th, 2022

DOI: <https://doi.org/10.21203/rs.3.rs-1212101/v1>

License:   This work is licensed under a Creative Commons Attribution 4.0 International License.

[Read Full License](#)

Single Particle Hopping as an Indicator for Evaluating Electrocatalysts

Jun-Gang Wang,¹ Linjuan Zhang,² Jing Xie,³ and Di Li^{*1, 4}

¹ School of Chemistry and Molecular Engineering, East China Normal University, Shanghai 200241, China

² Key Laboratory of Interfacial Physics and Technology, Shanghai Institute of Applied Physics, Chinese Academy of Sciences, Shanghai 201800, China

³ Institute of Microelectronics, Chinese Academy of Sciences, Beijing 100029, China

⁴ Key Laboratory of Bioorganic Phosphorus Chemistry & Chemical Biology, Department of Chemistry, Tsinghua University, Beijing, 10084, China

Abstract

Design and screening electrocatalysts for gas evolution reactions suffer from scanty understanding of multi-phase processes at the electrode-electrolyte interface. Due to the complexity of multi-phase interface, it is still a great challenge to capture gas evolution dynamics under operando condition to precisely portray the intrinsic catalytic performance of interface. Here, we establish a single particle imaging method to real time monitor a potential-dependent vertical motion or hopping of electrocatalysts induced by electrogenerated gas nanobubbles. The hopping feature of single particle is closely correlated with intrinsic activities of electrocatalysts, thus is developed to be an indicator to evaluate gas evolution performance of various electrocatalysts. This optical indicator diminishes interferences from heterogeneous morphologies, non-Faradaic processes and parasitic side reactions that are unavoidable in conventional electrochemical measurements, therefore enables precise evaluation and high-throughput screening of catalysts for gas evolution systems.

Introduction

Multi-phase interface in electrochemical reactions, where charge transfer and mass transport occur concomitantly at the electrode-electrolyte interfaces (EEl), plays a key role in understanding reaction mechanisms and is important for advancing renewable energy storage and conversion. The phase evolution generates unusual mass transport behavior, leading to a kinetic limitation of electrochemical processes. Moreover, this phase evolution is influenced by disorder of localized electric environment and spatiotemporal changes of heterogeneous morphology and electron transfer on electrode surface, thus is readily hidden by vast spectators and electrolytes.¹ As a result, a fundamental description of multi-phase interface evolution under polarization remains elusive. To take oxygen evolution reaction (OER) as an example, OER involves four-electron oxidation and complicated multi-phase processes, and is a sluggish kinetics in water splitting.² Therefore, it is urgently needed to accurately recognize the dynamics of phase evolution under operando condition³⁻⁶, which will facilitate a precise evaluation of intrinsic OER performance of various electrocatalysts.

Resolving the dynamic phase evolution during OER requires a technique with high spatiotemporal resolution and fast response towards catalytic events on electrocatalysts.^{7, 8} Conventional electrochemical measurements that widely used in characterizing electrocatalytic reactions suffer from inherent weaknesses of chemical identification and susceptibility to perturbation from non-Faradaic processes, such as double layer charging and concomitant spectator reactions, thereby are less efficient in recognizing the dynamic phase evolution process. Up to now, some advanced operando techniques^{9, 10}, including scanning probe microscope^{2, 11, 12}, mass spectrometry¹³⁻¹⁶, in situ infrared and Raman spectroscopy¹⁷, nuclear magnetic resonance^{18, 19} and X-ray based spectroscopy^{20, 21} have been developed to identify active species in electrochemical conversion and reveal catalytic mechanisms at atomic level.²² However, these characterizations still lack the capability of real time tracing phase change dynamics, particularly at the electrocatalyst-electrolyte-gas interface due to a short of either spatial resolution to follow individual electrocatalyst or temporal resolution to real time monitor OER event.²³

Optical imaging microscopy possesses advantages of superior spatiotemporal resolution and

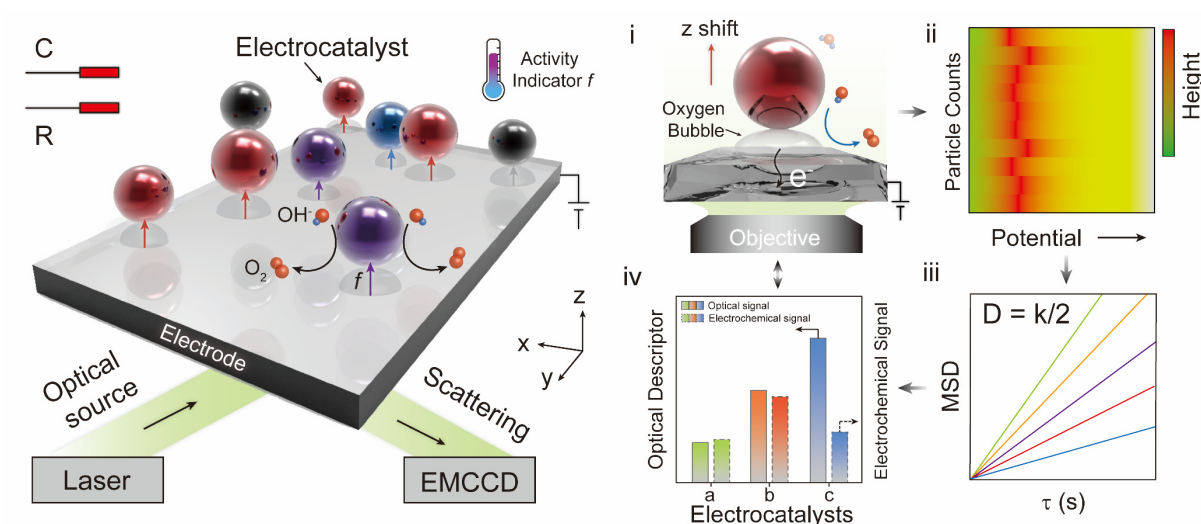


Fig. 1. Schematic illustration of the electrochemical generated gas bubble-induced vertical motion or hopping of electrocatalyst to evaluate their intrinsic activities. The hopping of electrocatalyst (i) is recorded through the attenuated scattering light intensity in evanescent field (ii). The hopping behavior of various electrocatalysts is then quantitated by their diffusion coefficient as obtained from the mean-square displacement (MSD) analysis (iii), normalized diffusion coefficient is developed as an optical indicator to define the intrinsic catalytic activity of various electrocatalysts (a-c) (iv).

negligible beam degradation, thus has been used to monitor interfacial reactions under operando condition including insulator to metal phase transition,^{24,25} energy flow and transport of chemical species,^{7,26} to identify reaction mechanisms²⁷⁻³². These implementations mostly rely on specific electronic or optical properties of systems, for instance, large Raman scattering cross-section, desirable emission or absorption and appreciable photostability.^{33,34} However, these imaging methods mainly focus on catalytic events occurred on focal plane, while electrochemical reactions could generate a concentration gradient of either substrate or product that perpendicular to electrode surface. Vertical motions of catalysts in this concentration gradient during OER may carry rich information about the multi-phase reaction dynamics, however, are largely ignored.

In the present study, we establish a correlative in situ electrochemical total internal reflection microscopy (EC-TIRM) imaging platform to visualize motion of electrocatalysts at multi-phase interface during OER. Particularly, by harnessing the depth-sensitive scattering intensity under total internal reflection illumination (< 200 nm, a comparison with other operando techniques was shown in Supplementary Table S1), this EC-TIRM resolves vertical motion of single electrocatalysts during gas evolution. We provide evidences of the existing of

heterogeneous electrogenerated oxygen nanobubbles with long lifetime and high mass density. The accumulating of supersaturated nanobubbles at solid-liquid interface, results in a vertical motion or hopping of electrocatalysts on electrode. We thus build a quantitative correlation between gas-induced hopping and OER performance of electrocatalysts (Fig. 1). The hopping of electrocatalysts is developed as an efficient indicator for accurate assessing and high-throughput screening of electrocatalysts for not only OER, but also most gas involving systems.

Results

Identification of Local Supersaturated Dissolved Oxygen Regions at EEIs. TIRM provides both wide and near field capability for imaging interfacial subjects, we thereby built a set of correlative EC-TIRM to visualize the dynamic phase evolution at EEIs during OER in order to corroborate the presence of local heterogeneous supersaturated regions at catalytic active sites readily for oxygen bubble nucleation and growth (Supplementary Fig. S1-S4). We first explored the liquid-gas phase change events, i.e., gas bubble nucleation and growth, on electrode surface. Rhodamine 6G (R6G) was introduced to label gas bubbles through hydrophobic interaction (Fig. 2a). A planar Cu substrate obtained from seed-mediated electrodeposition was used as an electrode for OER (Supplementary Fig. S2).³⁵ The adoption of a planar electrode instead of electrocatalyst particles-modified electrode, is based on the consideration to avoid interferences from particle scattering on R6G fluorescence.

The nucleation of gas bubble at liquid/solid interface leads to a trapping of R6G on the top of bubble^{1, 36, 37}, therefore the fluorescence spots of R6G enable to accurately identify local phase interface evolution regions without possible interferences caused by ex-situ analysis techniques and chemical additives.³⁸⁻⁴¹ The fluorescence of R6G was synchronized recorded with potential scan, as shown in Fig. 2b, bright spots occurred at a potential of 0.08 V (*vs* Pt quasi-reference electrode), then gradually disappeared after 0.50 V during anodic polarization, whereas increased again from 0.90 to 0 V in cathodic polarization. The fluorescence intensity time trajectories of several representative spots during dynamic potential scan were demonstrated in Fig. 2c. Considering the large energy barrier for nanobubble desorption from electrode and absence of supersaturated oxygen region in bulk electrolyte, the blinking features

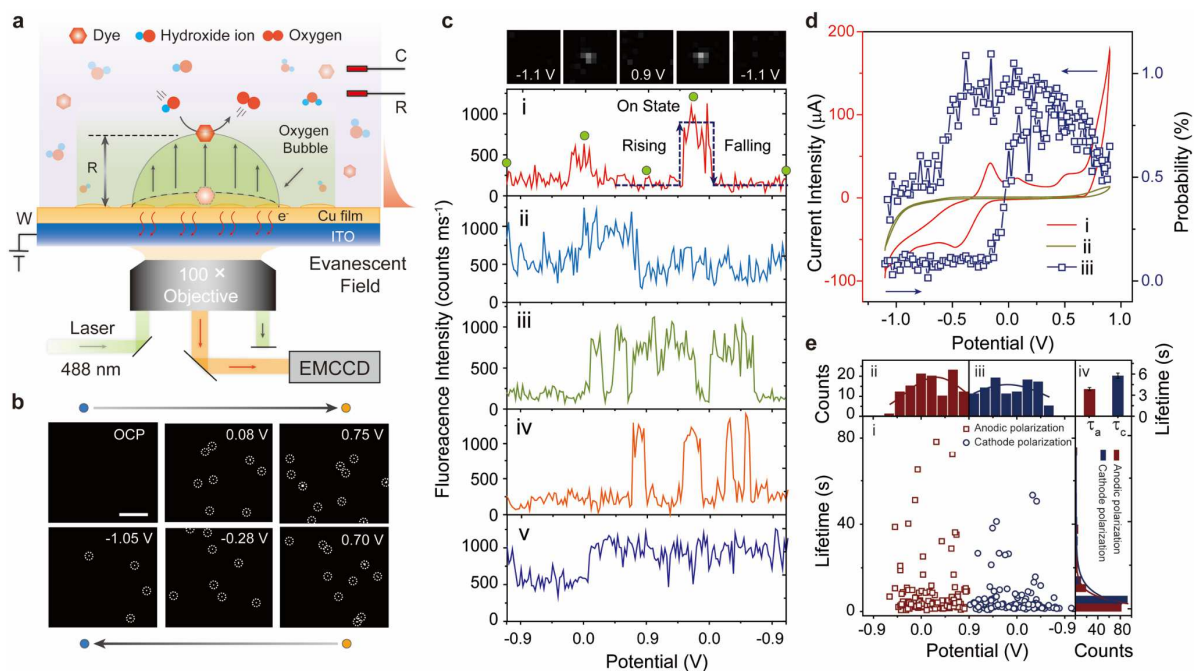


Fig. 2. Identification of local supersaturated dissolved oxygen regions at EEIs. (a) Schematic illustration of visualizing single R6G labeled gas bubble using correlative electrochemical total internal reflection microscopy (EC-TIRM). (b) A series of EC-TIRM images (19 × 17 μm² area) of oxygen nanobubble (highlighted by white dash circles) under various polarizations (open circuit potential (OCP); anodic polarization: 0.08, 0.75 V; cathodic polarization: 0.70, -0.28 and -1.05 V vs Pt) taken from consecutive potential scan from -1.10 to 0.90 then to -1.10 V on a Cu/ITO electrode, at a scan rate 0.10 V s⁻¹, in a solution containing 0.10 M KOH and 20 nM R6G (Scale bar, 5 μm). Fluorescence images were recorded at 4 frames s⁻¹ with a 100 ms exposure time. The center positions of nanobubble were super-localized with nanometer-scale precision through point spread function fitting. (c) Representative enlarged intensity trajectories for single oxygen bubble during dynamic potential scan (i-v). The representative potential dependent fluorescent images at different polarization potential (top panel) corresponding to the green dots in intensity trajectory (i). (d) Cyclic voltammograms of Cu/ITO electrode (i, red solid line), ITO (ii, green solid line) in 0.10 M KOH and the relative probability of bubble occurrence (events per frame/total events collected in all frames) for Cu/ITO electrode during dynamic potential scan (iii, blue square line) from -1.10 to 0.90 V, at a scan rate 0.10 V s⁻¹. (e) The lifetime of oxygen bubbles generated during dynamic potential scan (i), and the relative distribution of bubble lifetime under anodic polarization (ii) and cathodic polarization (iii). The lifetime of oxygen bubbles is fitted by a single-exponential decay function (iv).

in trajectories are only assigned to nanobubble nucleation and growth at the EEIs rather than escaping from the surface.³⁷ Four types of fluorescence fluctuations were observed, suggesting remarkable heterogeneity catalytic activities across the interface (Type i and ii fluctuations were collected for bubble lifetime statistical analysis, Supplementary Fig. S5-S6). Notably, the peak in potential-dependent fluorescence response in Fig. 2d suggested the presence of a competition between bubble nucleation and subsequent growth. Interestingly, the rise of fluorescence signal initiated (*ca.* 0 V) earlier than the onset potential in electrochemical measurement (*ca.* 0.60 V), indicating the existence of some highly active catalytic sites that

facilitate the heterogeneous oxygen bubble nucleation. When the coverage density of gas bubble was high (at 0.20 V), surrounding dissolved oxygen tends to diffuse to adjacent oxygen bubbles due to a high activation energy required for forming a new gas-liquid interface, resulting in the growth of gas bubble instead of heterogeneous nucleation of new bubbles, as shown by the gradual reduction of fluorescence signals from 0.20 V to 0.90 V.⁴²

The nucleation rate of oxygen bubbles as a function of applied potential could be modeled by classical nucleation theory (Fig. 2e and Supplementary Eq.7).^{43, 44} Notably, the size and lifetime distribution of gas bubble could be estimated from the variations of R6G fluorescence trajectories in the evanescent field.⁴⁵ The average lifetime of gas bubble was obtained from counting the blinking time of R6G fluorescence, and calculated to be 3.85 s and 5.77 s in anodic and subsequent cathodic polarization, respectively. The calculated bubble lifetimes were of 2 orders of magnitude longer than theory predicted values.^{46, 47} Because of the oversaturation region around gas bubbles, the mass transfer of gas molecule across the liquid-gas interface behaved as the limiting step in gas bubble's shrinkage and growth.⁴⁸ In order to clarify the origin of the prolonged lifetime, the surface bubble lifetime (t_b) was deduced according to an equilibrium between the oversaturation pressure and Laplace pressure (Eq. 1, and Supplementary Fig. S7):

$$t_b = \frac{L^2}{4D} \frac{\rho_b}{(\xi(t)+1)C_b} \quad (1)$$

where L is the footprint diameter of bubble (approximate to the diameter of gas bubble), D is diffusion coefficient of oxygen ($2.0 \times 10^{-9} \text{ m}^2 \text{ s}^{-1}$), $\xi(t)$ refers to oversaturation pressure, C_b is the solubility of oxygen in electrolyte (0.041 kg m^{-3}), ρ_b is the mass density of gas bubble.

From Eq. 1, we found that the lifetime of gas bubble is closely related to its mass density. After anodic potential scan, it was reasonable to assume that the oversaturation around the active catalytic sites remained a stable equilibrium, where $\xi(t)$ was considered as a constant. Noteworthy, the prolonged lifetime (5.77 s) and grown radius (63.40 nm) of oxygen bubble during subsequent cathodic potential scan led to a remarkable reduction of Laplace pressure on the bubble surface. In order to balance the force equilibrium, the mass density (ρ_b) in oxygen bubble during the cathodic polarization increased *ca.* 41 % compared to that in anodic polarization, which compensated the Laplace pressure and stabilized the force balance on the

bubble interface (detailed discussion shown in the Supplementary Information, Supplementary Fig. S8). The enhanced mass density in oxygen bubble was consistent with recent discovery of the presence of “dense gas” with in-situ synchrotron-based scanning transmission X-ray microscopy technique.⁴⁹ To further verify the saturated oxygen region, we performed finite element models (FEM) analysis to simulate the potential-dependent evolution of oxygen diffusion layer, and results suggested that the high potential scan rate used in the present study (0.10 V s^{-1}) facilitates the formation of a supersaturating region of oxygen and improves nanobubble nucleation and growth (Supplementary Fig. S9).

Oxygen bubble-Induced Single Electrocatalysts Hopping. Having confirmed the existence of saturated oxygen nanobubbles with long lifetime and high mass density at highly active catalytic interface, we then monitored the conceivable interfacial nanobubble evolution-induced electrocatalysts motion at reduced catalytic dimension (from two dimension to quasi-zero dimension) under operando condition using the correlative EC-TIRM through their elastic scattering signal (Fig. 3a and Supplementary Fig. S10). Briefly, under wide field illumination of 488 nm, the back-scattered light from the particle was collected by objective lens and imaged on EMCCD.⁵⁰ Here, a classical OER catalyst, IrO₂ particles with an average diameter of 200 nm (Supplementary Fig. S11), was used as a model system to demonstrate the oxygen nanobubble-induced motion of OER catalysts.⁵¹ The IrO₂ particles were drop-casted and sparsely dispersed on transparent ITO electrode, and the prominent current under anodic polarization revealed a remarkable oxygen evolution (Supplementary Fig. S11). It should be noted that we did not introduce R6G to label oxygen nanobubble in this IrO₂ system because the scattering of IrO₂ is extremely larger than the fluorescence of R6G. As a result, the fluorescence spot of R6G was invisible.

As shown in Fig. 3b, the scattering intensity of IrO₂ gradually decreased in a potential scan from - 0.30 V to 1.20 V (Supplementary video 1). In evanescent field, the scattering intensity of a subject is proportional to its distance from the interface (Fig. 3c). We thus speculated that the attenuation in scattering intensity of single IrO₂ particle was a result of vertical motion or hopping of IrO₂ caused by the propelling of high mass density gas bubbles generated at the

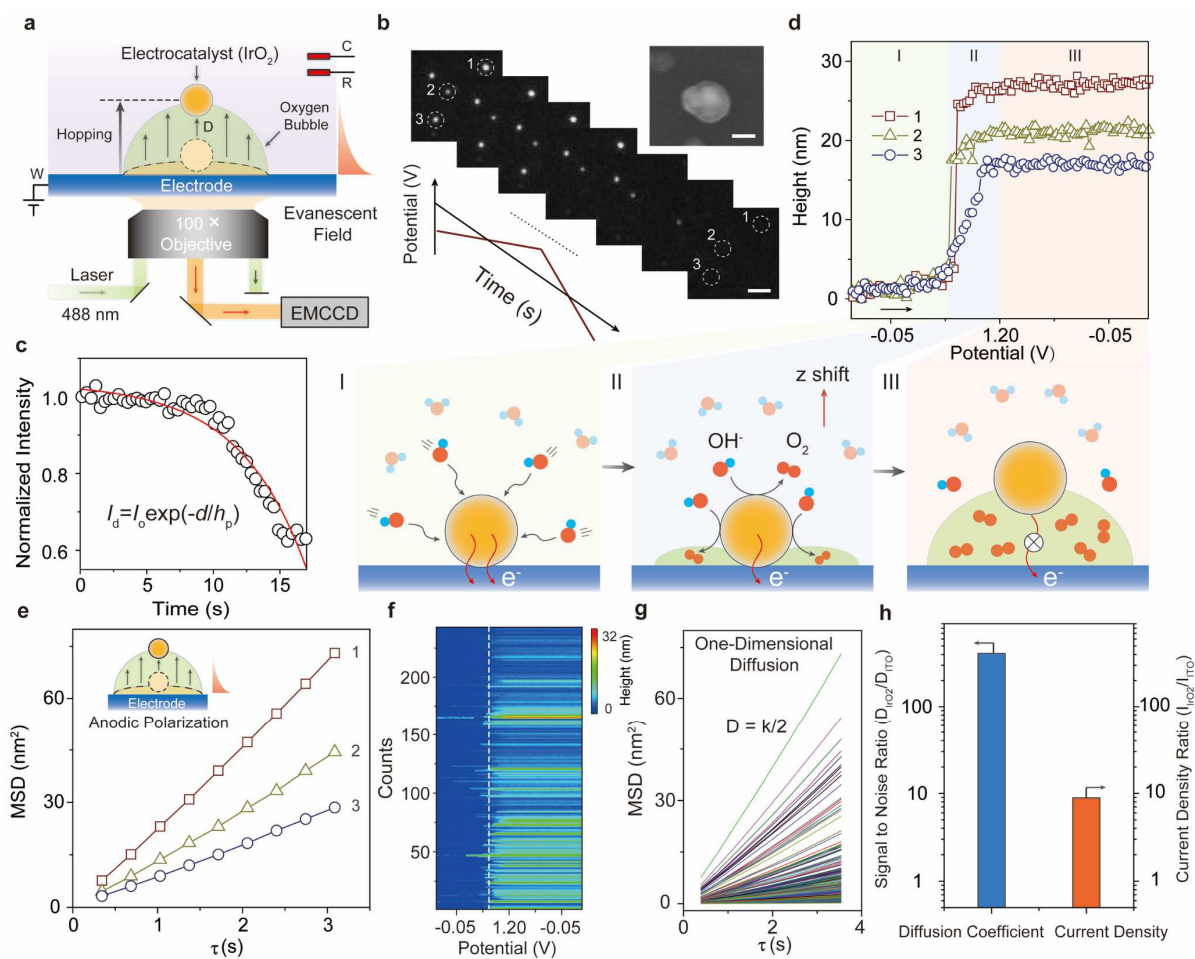


Fig. 3. Oxygen bubble-induced single electrocatalysts hopping. (a) Schematic of in situ EC-TIRM for monitoring the hopping of single particle. (b) Sequential scattering image of catalysts under polarization from -0.30 to 1.20 V (*vs* Pt) during OER, at a scan rate of 0.10 V s⁻¹, scale bar: 2 μm. Inset: Representative field emission scanning electron microscopy image of single IrO₂ particle. Scale bar: 100 nm. (c) The attenuation formulation between scattering intensity and position coordinate along perpendicular direction. The schematic shows the nanobubble-induced IrO₂ particle hopping behavior under different anodic polarization (I-III). (d) The height profiles of IrO₂ particles depicted by the white dash circle in (b) as a function of polarization potential. (e) The extracted mean-square displacement (MSD) curves along the vertical direction from representative particles depicted by the white dash circle in (b), based on the one-dimensional diffusion equation. (f) and (g) the statics of height evolution and corresponding MSD distribution. (h) Comparison the signal to noise ratio in optical and electrochemical approaches. The scattering intensity collected from dark region close to IrO₂ particle was adopted as background diffusion coefficient, and current density obtained at bare ITO electrode at 1.20 V was served as the background current density.

IrO₂/electrode interface (Supplementary Fig. S12-S14). In OER process, accompanied by increasing anodic polarization, excess positive charges are first accumulated on particle surface, which improve the adsorption of hydroxide through local electrostatic force and promote direct Faradaic transition from hydroxide to oxygen (Fig. 3d, I). Then, the gradual enrichment of oxygen species results in a formation of diffusion layer and an increase of chemical potential

of oxygen molecules near the particle surface. Upon the generation of supersaturated oxygen regions around individual particle, supersaturated state overcomes the activation energy barrier for nanobubble evolution, drives the heterogeneous nucleation and growth of nanobubbles that results in a lower local viscosity at the bottom of particle that eventually facilitate the dislocation of particle along the perpendicular direction of electrode surface (Fig. 3d, II). As the catalytic reaction ceases when the particle dissociates from the surface and shuts off the electron transfer pathway, the rapid attenuation of supersaturated oxygen layer around nanobubble accelerates the bubble breakage, thus providing supernumerary energy for the particle to overcome the energy barrier for desorption from the EEIs rather than recovering to its initial location (Fig. 3d, III).

We next performed a series of control experiments to verify this assumption. (1) The IrO₂ catalyzed OER was carried out at neutral environment, only weak fluctuation of IrO₂ scattering was observed (Supplementary Fig. S15). (2) The attenuated scattering of IrO₂ during OER was independent of illuminated laser wavelength and corresponding intensities (Supplementary Fig. S16). (3) OER was also performed on a catalytic inert SiO₂ sphere-modified ITO electrode, and the scattering of SiO₂ sphere also remained unchanged during OER (Supplementary Fig. S17-S18). (4) The attenuation of IrO₂ scattering was synchronized with oxygen evolution. Below the oxygen evolution potential where no phase transition was occurred, irreversible scattering intensity attenuation of IrO₂ was not observed (detailed discussion shown in Supplementary Fig. S19-S24). These control experiments indicated that the attenuation of IrO₂ scattering was closely related to multi-phase interface evolution during OER.

In addition, electrochemical charging of IrO₂ during dynamic potential scan may also result in a change of refractive index of its environment, leading to scattering intensity fluctuations. To exclude this possibility, cyclic voltammetry of IrO₂-modified electrode was carried out in a solution containing Fe(CN)₆³⁻/Fe(CN)₆⁴⁻ redox probe and the scattering of IrO₂ was monitored during continuous potential scans from - 0.50 V to 0.30 V and a periodic scattering change profile was observed (Supplementary Fig. S19-S24). The electrochemical charging and discharging-induced periodic scattering change profile was significantly different from the attenuation profile case in OER; therefore, this possibility was also ruled out. Moreover,

another possible explanation for scattering intensity fluctuation was the occurrence of O₂ bubble around IrO₂ particle surface. If this explanation is reasonable, a reversible scattering intensity change during successive potential scan is anticipated, however, we observed only a rapid scattering intensity decay in the first cycle scan under anodic polarization, and the scattering profile was irreversible under cathodic polarization. Meanwhile, the evaluated O₂ bubble could only enhance the scattering intensity of IrO₂ by increasing the apparent diameter of particle, which was clearly opposite to the attenuation results (Supplementary Fig. S25). All these control experiments suggested the attenuation of IrO₂ scattering intensity was a result of hopping of IrO₂ that induced by electrogenerated supersaturated nanobubble.

We then attempted to extract the diffusive information of IrO₂ from the scattering fluctuations. As illustrated in Eq. 2, the scattering intensity of a subject in evanescent field is proportional to its distance from interfaces:

$$I_d = I_0 \exp(-d/h_p) \quad (2)$$

Therefore, the scattering intensity fluctuations of IrO₂ during OER could be converted to its distance change away from electrode. To simplify the calculation, the nanobubble-induced hopping of IrO₂ was supposed to be perpendicular to electrode, while hopping with other angles was dismissed. The potential dependent vertical hopping height profiles of three representative individual particles (marked in Fig. 3b) were demonstrated in Fig. 3d. While lateral motion of particles was monitored by single particle tracking, the obtained confined motion trajectories excluded lateral motion from future analysis (Supplementary Fig. S25). Diffusion coefficient of the one-dimensional vertical motion could be extracted from mean square displacement (MSD) analysis of moving trajectories (Fig. 3e). MSD of three different IrO₂ particles in Fig. 3b revealed an almost linear increase over time, suggesting a Brownian behavior. Owing to the inhomogeneous growth of gas bubble, the hopping of different IrO₂ particles also revealed heterogeneity (Fig. 3f and g). Notably, the signal to noise ratio in the averaged diffusion coefficient of IrO₂ was significantly high (*ca.* 410 times), while the OER catalytic current at 1.20 V was only *ca.* 9 times higher than the background current (Fig. 3h). The bigger gap in diffusion coefficient indicated that the hopping of electrocatalysts could be a more sensitive parameter to evaluate the intrinsic OER performance of electrocatalysts (Supplementary Fig.

S26). These distinctive attributes from particle hopping enable detailed structure–function correlations in a broad range of materials and precisely recognizing the origin of composition and function heterogeneity in OER catalysts. Of note, due to sensitivity limit of EMCCD, only scattering profile of relatively large IrO₂ particles (> 100 nm) could be collected and analyzed. Our control experiments suggested catalytic activity of the IrO₂ electrode still possessed *ca.* 33 % after 10 scan cycles, suggesting the presence of some invisible IrO₂ particles on electrode that counts for the residual OER activity (Supplementary Fig. S14). The propose of the present study is to evaluate the OER activity of electrocatalysts from its departure from electrode surface, while the catalytic durability is not considered.

Electrocatalysts Hopping as an Indicator for Evaluating OER Performance. Having confirmed the supersaturated gas bubble induced hopping of single electrocatalyst on electrode, we next employed this hopping behavior to evaluate the intrinsic catalytic activity of various catalysts. We defined an indicator (f , Eq. 3) to describe the normalized oxygen bubble-induced electrocatalyst hopping,

$$f = \frac{\langle D \rangle}{A} \quad (3)$$

where $\langle D \rangle$ devotes to averaged diffusion coefficients of vertical motion of electrocatalysts, and A is the projected area of particle on electrode.

We then used this indicator to interrogate different OER catalysts. The first case is to study doping effect in transition metal oxides OER catalysts. Doping of foreign elements could regulate the local electronic structure of transition metal oxides and optimize the binding strength between active sites and hydroxyl ion on transition metal oxides, thus eventually enhance OER performance.^{52, 53} Calcium Cobalt oxide (Ca₃Co₄O₉), a promising a transition metal oxide for oxygen evolution, represents an archetypal system for studying elements doping on multi-phase interface evolution. We thus evaluated the OER performance of Ca₃Co₄O₉ with different doping (Supplementary Fig. S27-S28) with this indicator. Linear sweeping voltammetry (LSV) and Tafel plots of a series of catalysts were shown in Fig. 4a, the OER performance of different doping followed the order of Ca₃Co_{3.2}Fe_{0.8}O₉ > Ca₃Co₄O₉ > Co₃O₄ from Fig. 4b and c.

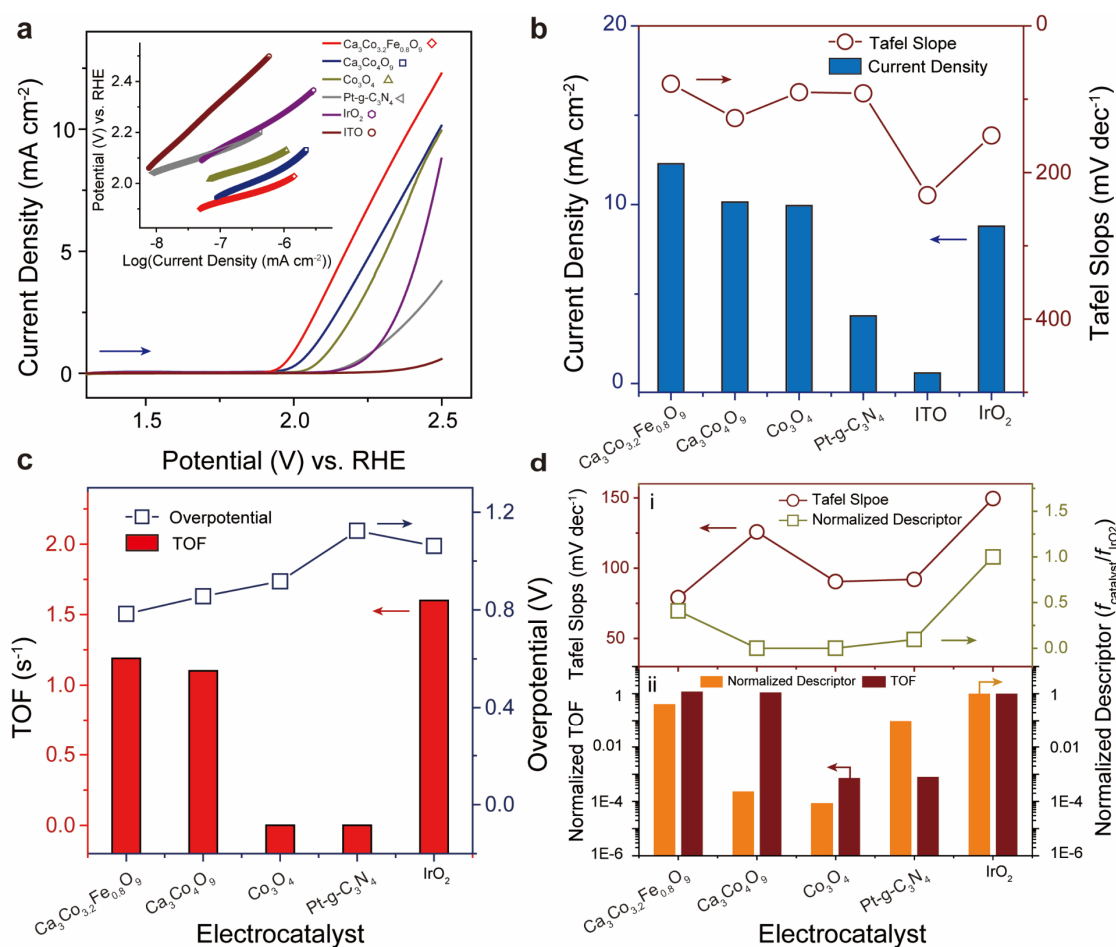


Fig. 4. Electrocatalysts hopping as an Indicator for evaluating OER performance. Correlation of electrochemical parameters and optical indicator among various electrocatalysts. (a) Linear potential scan during potential scan from 0 to 2.50 V vs RHE for series catalysts in 0.10 M KOH aqueous solution at a scan rate of 0.10 V s⁻¹. Inset indicates corresponding Tafel slopes. (b) Comparison of Tafel slope and current density at 2.50 V vs RHE of various catalysts. (c) Comparison of TOF value (numbers of oxygen molecule converted per second) and oxygen evolution overpotential at a current density 2.5 mA cm⁻². (d) The normalized indicator ($f_{\text{catalyst}}/f_{\text{IrO}_2}$) compared with Tafel slopes (upper panel) and normalized TOF value ($\text{TOF}_{\text{catalyst}}/\text{TOF}_{\text{IrO}_2}$) of various catalysts (bottom panel).

We monitored the hopping of these catalysts and the corresponding f values were calculated to be $6.9 \times 10^{-6} \text{ s}^{-1}$ and $3.9 \times 10^{-9} \text{ s}^{-1}$ for $\text{Ca}_3\text{Co}_{3.2}\text{Fe}_{0.8}\text{O}_9$ and $\text{Ca}_3\text{Co}_4\text{O}_9$, respectively (Supplementary Fig. S29-S33). The order of $\text{Ca}_3\text{Co}_{3.2}\text{Fe}_{0.8}\text{O}_9 > \text{Ca}_3\text{Co}_4\text{O}_9$ well matched the results from Tafel plots (79 and 125 mV dec⁻¹) and TOF values (1.19 and 1.10 s^{-1}). The enhanced catalytic activity by Fe doping was assigned to the modification of intrinsic electric structure that decrease the hydroxyl adsorption activation energy on Co active sites and increase anisotropic electron conduction, as confirmed by electrochemical impedance spectroscopy and synchrotron X-ray adsorption spectroscopy results.^{54, 55}

However, the order of Co_3O_4 was inconsistent in electrochemical and optical tests. Co_3O_4 possessed a lower f value as compared to $\text{Ca}_3\text{Co}_4\text{O}_9$, while its current was similar with $\text{Ca}_3\text{Co}_4\text{O}_9$. We argued that the OER current of Co_3O_4 involves non-efficient Faradaic contribution. Co_3O_4 exhibits two bulk redox transformations with increasing anodic polarization at $E_1 \approx 1.60$ V and $E_2 \approx 1.85$ V (*vs* reversible hydrogen electrode (RHE)), which are assigned to the conversion of Co(II) to Co(III) and Co(III) to Co(IV), respectively (Supplementary Fig. S34).⁵⁶ To investigate the influence of redox state transformations on OER performance, we performed kinetic measurements at different potential scan rate during 1.20 and 1.90 V. A scan rate-dependent relationship for coupled redox peaks revealed that Co atom was quasi-reversibly oxidized and reduced in this pre-catalytic region, which can be explained as the restraint of inherent charge transfer property of Co species, rather than supply of reactants from bulk electrolyte under polarization.³⁵ Notably, OER begins concomitantly with the second bulk redox process at $E > 1.80$ V (Supplementary Fig. S34), indicating the presence of supererogatory charge contribution from redox couple transformation rather than absolute Faradaic transition from hydroxide ion to oxygen. Considering these perturbations on accurate evaluation of OER efficiency, it requires to eliminate these non-efficient contributions from OER performance. In contrast, the scattering optical response is independent of chemical transition and ions intercalation of interface compositions. As a result, we found that the average onset potential for Co_3O_4 hopping exhibits a slight lag behind *ca.* 0.28 V compared to that in electrochemical measurements. In contrast to the high Co atom proportion in Co_3O_4 (*ca.* 43 %), the lower Co atom proportion (*ca.* 25 % for $\text{Ca}_3\text{Co}_4\text{O}_9$, and *ca.* 19 % for doping species), gives a negligible redox transition contribution on OER evaluation, where the doping induced thermodynamic property improvements play a dominate role in OER performance. These results suggested that single particle hopping measurements enable us to accurately recognize intrinsic onset potential of OER and facilitate to preclude non-efficient Faradaic contribution to OER performance from redox state transformation, which cannot be excluded from traditional electrochemical approaches.⁵⁷

The second case is to explore morphology feature of electrocatalysts on OER with Pt nanoparticles decorated on *g*- C_3N_4 (Pt-*g*- C_3N_4) nanosheets (Supplementary Fig. S35-S37). The

morphological heterogeneity of layer structure results in a *ca.* 120 times enhancement in the optical indicator over TOF value of Pt-g-C₃N₄-modified electrode (Fig. 4d). Notably, the onset potential in hopping measurement (1.87 V) exhibited *ca.* 130 mV earlier than LSV results (2.00 V) (Supplementary Fig. S38). We argued that the higher catalytic activity in hopping measurement might arise from two factors, i.e., electronic conduction and mass transfer pattern. For single layer of Pt-g-C₃N₄ nanosheet, Pt nanoparticles not only provides abundant spaces for hydroxide ion adsorption, but also accelerates the subsequent charge transfer and quasi-sphere mass transport to facilitate OER proceeding, whereas the morphology of bulk Pt-g-C₃N₄ electrode exhibited flat topography with a thickness of *ca.* 460 nm (Supplementary Fig. S39-S40). The pile of Pt-g-C₃N₄ nanosheets on electrode not only blocks the vertical charge transport from electrode to electrolyte, but also changes the mass transfer pattern to an insufficient two-plane diffusion mode that limits diffusion of OH⁻ towards electrode surface (finite element simulations shown in Supplementary Fig. S41). These results confirmed previous hypothesis of pursuing single particle or even supreme single atom dispersion that expose sufficient active sites and electronic conductivity pathways to achieve prominent improvement of OER performance by eliminating ensemble morphology limitations.⁵⁸

Discussion

In conclusion, we developed an indicator to accurately define the intrinsic catalytic activity of OER catalysts. This indicator was derived from the hopping of electrocatalysts on electrode under operando condition. Benefitting from the depth-sensitive EC-TIRM, the vertical motion behaviors of electrocatalysts during OER were investigated. This indicator diminishes interferences from morphology, non-efficient Faradaic effects and concomitant chemical reactions on Faradaic processes, enabling to establish an accurate correlation with the inherent activity in a broad range of materials. We envision that the proposed strategy is important for providing a complement of existing operando methodologies for high-throughput screening of catalysts for OER as well as more complex gas-evolving systems. Moreover, the concept of motion-activity relationship, instead of structure-activity relationship, may shed new light on investigation their contributions to catalysts.

Methods

Instruments. Time-of-Flight secondary ion mass spectrometry (ToF-SIMS) measurements were performed using a ToF-SIMS V (ION-TOF GmbH, Münster, Germany) mass spectrometer equipped with a time-of-flight analyzer of a reflectron type. A 30 keV Bi_3^+ primary ion beam was used at 10 kHz frequency with a pulsed beam current of 0.36 pA, and it was focused to be ~ 450 nm diameter in fast imaging mode to proceed chemical species imaging. All ion images resolution was 512×512 pixels. The negative and positive mass spectra were calibrated by CH_3^+ , H_3O^+ and NH_4^+ and C^- , OH^- and C_2^- , respectively. The vacuum pressure in the main chamber during the measurements was below 3×10^{-9} mbar. UV-Vis spectra were achieved on a UV-2600 spectrophotometer (Shimadzu, Japan). Sizes distributions were detected using dynamic light scattering (DLS) in Malven Zetasiwer Nano-ZS90. AFM measurements were performed on a Bioscope Resolve AFM (Bruker Corp., USA) under tapping mode with a scan rate of 1.0 Hz frequency. AFM images with a resolution of 512×512 pixels were acquired using silicon cantilevers with a normal spring constant of 0.35 N m^{-1} . All recorded AFM images were conducted by “Flatten” function prior to analysis in NanoScope Analysis software (version 1.60). X-ray diffraction (XRD) patterns were collected on a Bruker D8-ADVANCE X-ray diffractometer with DteX Ultra 250 detector and copper target using monochromatic $\text{Cu K}\alpha$ radiation ($\lambda = 1.5406 \text{ \AA}$). The range of diffraction (Bragg) angles were measured within the scan range from 10° to 60° with a step angle of 0.02° and a scan rate of $20^\circ \text{ min}^{-1}$ at 40 KV, 30 mA. The incident Soller slit and length-limiting slit was set as 2.5° and 5 mm, respectively. Field Emission transmission electron microscope (TEM) images were collected on JEOL-2100F (Japan) equipped with an energy dispersive X-ray detector and operated at voltage 200 kV. High-resolution TEM images and relative elemental mapping were carried out during HRTEM measurements. For TEM characterization, the catalyst nanoparticles ($5 \mu\text{g}$) were gently dispersed in aqueous solution ($200 \mu\text{L}$) by sonication (10 min). Then, a droplet of the suspension with $20 \mu\text{L}$ was gently dropped onto a carbon coated-copper grid (300 mesh), allowing the solvent to evaporate prior to imaging. The surface morphology analysis of the samples and energy dispersive X-ray (EDAX) mapping analysis were carried

out using field emission-scanning electron microscopy (FE-SEM) (Zeiss Gemini 450, Jena, Germany) fitted with an Oxford Symmetry Electron Back Scattering Diffraction (EBSD) detector. For cross-sectional FE-SEM, side-view images of Pt-g-C₃N₄ modified ITO substrate (cut from a bulk electrode by using a diamond pencil) were collected.

EC-TIRM Analysis. In situ EC-TIRM experiments were performed on a confocal fluorescence microscope (Nikon Ti2-E) equipped with Z-drive and Perfect Focus System (PFS) autofocus mechanisms that ensured a better focus stability and avoided long-term focus drift during continuous dynamic potential scan. The detector was equipped with an iXon EMCCD camera (897) controlled by NIS-Elements software. The excitation laser 488 nm passed through the excitation filter (502–549 nm) and was directed into an oil-immersion objective (CFI Apochromat TIRF 100XH Oil, NA 1.49, W.D. 0.12 mm). The built-in 1.5× zoom-in adaptor enables a magnification factor of 150×. An exposure time of 100 ms per frame was used. The delay between frames was 15 ms. After 10 s collection of the TIRM images at open circuit potential, the in situ TIRM images were recorded under dynamic potential scan from -1.10 to 0.90 V (*vs* Pt), at a scan rate of 0.10 V s⁻¹. Briefly, upon wide field illumination at a wavelength of 488 nm (E_i), the back-scattered light from the particle (E_s) was collected by objective lens and imaged on EMCCD. The TIRM images were analyzed using ImageJ software. The shading correction and background correction were applied on the original images. The central position of individual emitters was determined through fitting with a two-dimensional (2D) Gaussian function.

Data availability

The data that support the findings of this study are available from the corresponding author upon reasonable request.

References

1. Angulo A., van der Linde P., Gardeniers H., Modestino M., Fernández Rivas D., Influence of Bubbles on the Energy Conversion Efficiency of Electrochemical Reactors. *Joule* **4**, 555-579 (2020).

2. Mefford J. T. *et al.*, Correlative Operando Microscopy of Oxygen Evolution Electrocatalysts. *Nature* **593**, 67-73 (2021).
3. Wang H. *et al.*, Strong Metal–Support Interactions on Gold Nanoparticle Catalysts Achieved through Le Chatelier’s Principle. *Nat. Catal.* **4**, 418-424 (2021).
4. Huang J. *et al.*, Manipulating Atomic Structures at the Au/TiO₂ Interface for O₂ Activation. *J. Am. Chem. Soc.* **142**, 6456-6460 (2020).
5. Li J., Gong J., Operando Characterization Techniques for Electrocatalysis. *Energy Environ. Sci.* **13**, 3748-3779 (2020).
6. Zhang Z., Zandkarimi B., Alexandrova A. N., Ensembles of Metastable States Govern Heterogeneous Catalysis on Dynamic Interfaces. *Acc. Chem. Res.* **53**, 447-458 (2020).
7. Delor M., Weaver H. L., Yu Q., Ginsberg N. S., Imaging Material Functionality through Three-Dimensional Nanoscale Tracking of Energy Flow. *Nat. Mater.* **19**, 56-62 (2020).
8. Voiry D. *et al.*, Best Practices for Reporting Electrocatalytic Performance of Nanomaterials. *ACS Nano* **12**, 9635-9638 (2018).
9. Zhu Y., Wang J., Chu H., Chu Y. -C., Chen H. M., In Situ/Operando Studies for Designing Next-Generation Electrocatalysts. *ACS Energy Lett.* **5**, 1281-1291 (2020).
10. Li J., Peng Z., Wang E., Tackling Grand Challenges of the 21st Century with Electroanalytical Chemistry. *J. Am. Chem. Soc.* **140**, 10629-10638 (2018).
11. Simon G. H., Kley C. S., Roldan Cuenya B., Potential-Dependent Morphology of Copper Catalysts During CO₂ Electroreduction Revealed by In Situ Atomic Force Microscopy. *Angew. Chem., Int. Ed.* **60**, 2561-2568 (2021).
12. Zhang W. *et al.*, Kinetic Pathways of Ionic Transport in Fast-Charging Lithium Titanate. *Science* **367**, 1030-1034 (2020).
13. Wang J. -G. *et al.*, Direct Molecular Evidence of Proton Transfer and Mass Dynamics at the Electrode–Electrolyte Interface. *J. Phys. Chem. Lett.* **10**, 251-258 (2019).
14. Peng Z., Freunberger S. A., Chen Y., Bruce P. G., A Reversible and Higher-Rate LiO₂ Battery. *Science* **337**, 563 (2012).
15. Zhou Y. *et al.*, Real-Time Mass Spectrometric Characterization of the Solid–Electrolyte Interphase of a Lithium-Ion Battery. *Nat. Nanotechnol.* **15**, 224-230 (2020).

16. Huang J., Scott S. B., Chorkendorff I., Wen Z., Online Electrochemistry–Mass Spectrometry Evaluation of the Acidic Oxygen Evolution Reaction at Supported Catalysts. *ACS Catal.* **11**, 12745-12753 (2021).
17. Wang X., Huang S. -C., Hu S., Yan S., Ren B., Fundamental Understanding and Applications of Plasmon-Enhanced Raman Spectroscopy. *Nat. Rev. Phys.* **2**, 253-271 (2020).
18. Xiang Y. *et al.*, Visualizing the Growth Process of Sodium Microstructures in Sodium Batteries by in-situ ^{23}Na MRI and NMR Spectroscopy. *Nat. Nanotechnol.* **15**, 883–890 (2020).
19. Bhattacharyya R., Key B., Chen H., Best A. S., Hollenkamp A. F., Grey C. P., In situ NMR Observation of the Formation of Metallic Lithium Microstructures in Lithium Batteries. *Nat. Mater.* **9**, 504-510 (2010).
20. Singer A. *et al.*, Nucleation of Dislocations and Their Dynamics in Layered Oxide Cathode Materials during Battery Charging. *Nat. Energy* **3**, 641-647 (2018).
21. Zhou, J. *et al.*, Voltage- and Time-dependent Valence State Transition in Cobalt Oxide Catalysts during the Oxygen Evolution Reaction. *Nat. Commun.* **11**, 1984 (2020).
22. Tang Z., Zhao S., Yang Y., Insight into Structural Evolution, Active Site and Stability of Heterogeneous Electrocatalysts. *Angew. Chem., Int. Ed.* DOI: 10.1002/anie.202110186 (2021).
23. Yu Y. -S. *et al.*, Three-Dimensional Localization of Nanoscale Battery Reactions using Soft X-Ray Tomography. *Nat. Commun.* **9**, 921 (2018).
24. Yuan T., Wei W., Jiang W., Wang W., Vertical Diffusion of Ions within Single Particles during Electrochemical Charging. *ACS Nano* **15**, 3522-3528 (2021).
25. Jin Y. *et al.*, In Operando Plasmonic Monitoring of Electrochemical Evolution of Lithium Metal. *Proc. Natl. Acad. Sci. U. S. A.* **115**, 11168 (2018).
26. Merryweather A. J., Schnedermann C., Jacquet Q., Grey C. P., Rao A., Operando Optical Tracking of Single-Particle Ion Dynamics in Batteries. *Nature* **594**, 522-528 (2021).
27. Li Y., Yang C., Guo X., Single-Molecule Electrical Detection: A Promising Route toward the Fundamental Limits of Chemistry and Life Science. *Acc. Chem. Res.* **53**, 159-169

- (2020).
28. Wang J. -G., Jing C., Long Y. -T., Single-Nanoparticle Plasmonic Spectroelectrochemistry. In: *Frontiers of Plasmon Enhanced Spectroscopy Volume 2*). American Chemical Society (2016).
 29. Hoener B. S. *et al.*, Plasmonic Sensing and Control of Single-Nanoparticle Electrochemistry. *Chem* **4**, 1560-1585 (2018).
 30. Li W. *et al.*, Single-Molecular Catalysis Identifying Activation Energy of the Intermediate Product and Rate-Limiting Step in Plasmonic Photocatalysis. *Nano Lett.* **20**, 2507-2513 (2020).
 31. Judge W. D., Paeng J., Azimi G., Electrorefining for Direct Decarburization of Molten Iron. *Nat. Mater.* DOI: 10.1038/s41563-021-01106-z (2021).
 32. Li S. *et al.*, Nanobubbles: An Effective Way to Study Gas-Generating Catalysis on a Single Nanoparticle. *J. Am. Chem. Soc.* **139**, 14277-14284 (2017).
 33. Penwell S. B., Ginsberg L. D. S., Noriega R., Ginsberg N. S., Resolving Ultrafast Exciton Migration in Organic Solids at the Nanoscale. *Nat. Mater.* **16**, 1136-1141 (2017).
 34. Xin N. *et al.*, Concepts in the Design and Engineering of Single-Molecule Electronic Devices. *Nat. Rev. Phys.* **1**, 211-230 (2019).
 35. Wang J. -G. *et al.*, In-situ Plasmonic Tracking Oxygen Evolution Reveals Multistage Oxygen Diffusion and Accumulating Inhibition. *Nat. Commun.* **12**, 2164 (2021).
 36. Chan C. U., Ohl C. -D., Total-Internal-Reflection-Fluorescence Microscopy for the Study of Nanobubble Dynamics. *Phys. Rev. Lett.* **109**, 174501 (2012).
 37. Hao R., Fan Y., Howard M. D., Vaughan J. C., Zhang B., Imaging Nanobubble Nucleation and Hydrogen Spillover during Electrocatalytic Water Splitting. *Proc. Natl. Acad. Sci. U. S. A.* **115**, 5878 (2018).
 38. Mao X., Liu C., Hesari M., Zou N., Chen P., Super-Resolution Imaging of Non-Fluorescent Reactions via Competition. *Nat. Chem.* **11**, 687-694 (2019).
 39. Xiao X., Bard A. J., Observing Single Nanoparticle Collisions at an Ultramicroelectrode by Electrocatalytic Amplification. *J. Am. Chem. Soc.* **129**, 9610-9612 (2007).
 40. Zwaschka G., Nahalka I., Marchioro A., Tong Y., Roke S., Campen R. K., Imaging the

- Heterogeneity of the Oxygen Evolution Reaction on Gold Electrodes Operando: Activity is Highly Local. *ACS Catal.* **10**, 6084-6093 (2020).
41. Chen J. *et al.*, Measuring the Activation Energy barrier for the Nucleation of Single Nanosized Vapor Bubbles. *Proc. Natl. Acad. Sci. U. S. A.* **116**, 12678 (2019).
 42. Hao R., Fan Y., Anderson T. J., Zhang B., Imaging Single Nanobubbles of H₂ and O₂ During the Overall Water Electrolysis with Single-Molecule Fluorescence Microscopy. *Anal. Chem.* **92**, 3682-3688 (2020).
 43. Edwards M. A., White H. S., Ren H., Voltammetric Determination of the Stochastic Formation Rate and Geometry of Individual H₂, N₂, and O₂ Bubble Nuclei. *ACS Nano* **13**, 6330-6340 (2019).
 44. Taqieddin A., Allshouse M. R., Alshawabkeh A. N., Review-Mathematical Formulations of Electrochemically Gas-Evolving Systems. *J. Electrochem. Soc.* **165**, E694-E711 (2018).
 45. Fish K. N., Total Internal Reflection Fluorescence (TIRF) Microscopy. *Curr. Protoc. Cytom.* **50**, 12.18.11-12.18.13 (2009).
 46. Lohse D., Zhang X., Surface Nanobubbles and Nanodroplets. *Rev. Mod. Phys.* **87**, 981-1035 (2015).
 47. Tan B. H., An H, Ohl C. -D., How Bulk Nanobubbles Might Survive. *Phys. Rev. Lett.* **124**, 134503 (2020).
 48. Kurotani Y., Tanaka H., A Novel Physical Mechanism of Liquid Flow Slippage on a Solid Surface. *Sci. Adv.* **6**, eaaz0504 (2020).
 49. Zhou L. *et al.*, Ultrahigh Density of Gas Molecules Confined in Surface Nanobubbles in Ambient Water. *J. Am. Chem. Soc.* **142**, 5583-5593 (2020).
 50. Ortega Arroyo J., Cole D., Kukura P., Interferometric Scattering Microscopy and its Combination with Single-Molecule Fluorescence Imaging. *Nat. Protoc.* **11**, 617-633 (2016).
 51. McCrory C. C. L., Jung S., Peters J. C., Jaramillo T. F., Benchmarking Heterogeneous Electrocatalysts for the Oxygen Evolution Reaction. *J. Am. Chem. Soc.* **135**, 16977-16987 (2013).
 52. Zhang B. *et al.*, Homogeneously Dispersed Multimetal Oxygen-Evolving Catalysts.. *Science* **352**, 333-337 (2016).

53. Hao J. *et al.*, Discharge-Induced Enhancement of the Oxygen Evolution Reaction. *Angew. Chem., Int. Ed.* **60**, 20042-20048 (2021).
54. Lin X. *et al.*, An Efficient Family of Misfit-Layered Calcium Cobalt Oxide Catalyst for Oxygen Evolution Reaction. *Adv. Mater. Interfaces* **5**, 1801281 (2018).
55. Deng X., Sorescu D. C., Waluyo I., Hunt A., Kauffman D. R., Bulk vs Intrinsic Activity of NiFeO_x Electrocatalysts in the Oxygen Evolution Reaction: The Influence of Catalyst Loading, Morphology, and Support Material. *ACS Catal.* **10**, 11768-11778 (2020).
56. Kim T. W., Woo M. A., Regis M., Choi K. -S., Electrochemical Synthesis of Spinel Type ZnCo₂O₄ Electrodes for Use as Oxygen Evolution Reaction Catalysts. *J. Phys. Chem. Lett.* **5**, 2370-2374 (2014).
57. Brasiliense V. *et al.*, Monitoring Cobalt-Oxide Single Particle Electrochemistry with Subdiffraction Accuracy. *Anal. Chem.* **90**, 7341-7348 (2018).
58. Wang A., Li J., Zhang T., Heterogeneous Single-Atom Catalysis. *Nat. Rev. Chem.* **2**, 65-81 (2018).

Acknowledgements

This work was supported by the National Natural Science Foundation of China (21874046, 21902050, 22179141), National Postdoctoral Program for Innovative Talents (BX20190118), Shanghai Post-Doctoral Excellence Program (2019220), Shanghai Municipal Commission for Science and Technology (19JC1411800), the Fundamental Research Funds for the Central Universities, the original innovation project from 0 to 1 of the Basic Frontier Scientific Research Program (ZDBS-LY-JSC010) and DNL Cooperation Fund (DNL202008) of the Chinese Academy of Sciences.

Author contributions

J.-G. W. and D. L. designed research; J.-G. W. and D. L. performed research; J.-G. W., L. Z., J. X. and D. L. analyzed data; J.-G. W. and D. L. wrote the paper.

Corresponding author

Di Li

Email: dli@chem.ecnu.edu.cn;

ORCID: D. L.: 0000-0003-1674-0110

Competing interests

The authors declare no competing interests.

Additional information

Supplementary information is available for this paper.

Supplementary Files

This is a list of supplementary files associated with this preprint. Click to download.

- [VideoS1.avi](#)
- [SupplementaryInformation20211228NC.docx](#)